Journal of Ceramic Processing Research. Vol. 27, No. 1, pp. 37~47 (2026)
(Received 13 August 2025, Received in revised form 1 November 2025, Accepted 6 November 2025)
https://doi.org/10.36410/jcpr.2026.27.1.37

J O U R N A L O F
Ceramic Processing Research

Cobalt-modified $Mg_{0.95}Zn_{0.05}TiO_3$ ceramics with improved dielectric properties for microwave applications

Ruei-Sung Yu[a], Cheng-Che Ho[b], Chun-Hong Chen[c], Yao-Chin Wang[d], Che-Hao Liao[b], Po-Cheng Chen[b] and Shih-Hung Lin[b,*]

[a]*Department of Chemical and Materials Engineering, National Chin-Yi University of Technology, No.57, Sec. 2, Zhongshan Rd., Taiping Dist., Taichung 411030, Taiwan*
[b]*Department of Electronic Engineering, National Yunlin University of Science and Technology, 123 University Road, Section 3, Douliou, Yunlin 64002, Taiwan*
[c]*Department of Electrical Engineering, National Chung Cheng University, Chiayi, Taiwan*
[d]*Department of Electronic Engineering, Cheng Shiu University, Kaohsiung, Taiwan*

In pursuit of high-performance and energy-efficient dielectric ceramics for next-generation wireless communication systems, this work examines the effect of Co^{2+} substitution for Mg^{2+} on the microstructure and microwave dielectric properties of $(Mg_{0.95}Zn_{0.05})TiO_3$ ceramics. A series of $[(Mg_{1-x}Co_x)_{0.95}Zn_{0.05}]TiO_3$ compositions (x = 0.1–0.4) was synthesized via solid-state reaction and characterized by synchrotron XRD, Raman spectroscopy, SEM, and dielectric measurements. The optimal composition, $[(Mg_{0.8}Co_{0.2})_{0.95}Zn_{0.05}]TiO_3$, sintered at 1350 °C for 2 h, achieved ε_r = 18.42, Qf = 190,000 GHz, and τ_f = −51 ppm/°C, representing a 16.2% Qf enhancement and a 43.7% reduction in overall thermal budget compared with literature benchmarks. These results are attributed to improved densification, increased lattice polarizability, and a stable phase composition. The findings demonstrate a viable route toward low-loss, energy-efficient microwave ceramics suitable for 5G and future communication devices.

Keywords: Crystallization, Dielectric performance, Microwave ceramics, Energy-efficient processing, 5G applications.

Introduction

The rapid development of fifth-generation (5G) and beyond 5G (B5G) communication technologies has imposed stringent demands on dielectric materials used in microwave components such as resonators, filters, antennas, and substrates. These materials must offer high performance—such as low dielectric loss, high permittivity, and thermal stability—and low-cost and energy-efficient processing to meet industrial scalability and sustainability requirements [1–14]. Among the critical microwave dielectric properties, dielectric permittivity (ε_r), quality factor (Qf), and temperature coefficient of resonant frequency (τ_f) are the key parameters that determine signal selectivity, miniaturization, and long-term device reliability [15–25].

$MgTiO_3$-based ceramics, with an ilmenite-type structure, are widely studied for microwave applications owing to their high Qf values and moderate ε_r. However, conventional $MgTiO_3$ materials typically require high sintering temperatures (~1400 °C for 4 h), resulting in excessive energy consumption and abnormal grain growth that can deteriorate microstructural uniformity [26–29]. To overcome these limitations, various modification strategies have been developed to enhance densification and dielectric performance at reduced firing temperatures. For example, cation substitution has proven effective in stabilizing the lattice and improving microwave properties, as demonstrated in Ni/Sb-modified Mg_2TiO_4 ceramics and Zn/Sn-cosubstituted $MgTiO_3$-based systems [30, 31]. These studies indicate that appropriate cation engineering can significantly lower the thermal budget while maintaining excellent dielectric properties suitable for microwave applications.

Recent studies have explored cation substitution at the A-site (Mg^{2+}) as a strategy to improve densification and dielectric properties. Cobalt (Co^{2+}), with an ionic radius similar to that of Mg^{2+}, has shown promise in enhancing Qf and enabling improved microstructural control [32]. For example, $Mg_{0.95}Co_{0.05}TiO_3$ sintered at 1450 °C for 4 h exhibits a Qf of 230,000 GHz and τ_f of −54 ppm/°C, outperforming undoped $MgTiO_3$. Meanwhile, co-substitution with Zn^{2+} has also been shown to lower sintering temperatures while maintaining satisfactory dielectric properties. Huang et al. reported that $[(Mg_{0.7}Zn_{0.3})_{0.95}Co_{0.05}]TiO_3$ sintered at 1200 °C for 4 h achieved $\varepsilon_r \approx 20.0$ and $Qf \approx 163{,}560$ GHz [33].

Despite these promising developments, two critical

*Corresponding author:
Tel : +886-5-5342601 (ext. 4344)
Fax: +886-5-5312063
E-mail: isshokenmei@yuntech.edu.tw

challenges remain. First, the formation of secondary phases, such as $[(Mg_{1-x}Co_x)_{0.95}Zn_{0.05}]_2TiO_4$ and $[(Mg_{1-x}Co_x)_{0.95}Zn_{0.05}]Ti_2O_5$, under elevated sintering temperatures or high Co concentrations, is not fully understood. These phases may introduce interfacial defects, increase dielectric loss, and impair densification. Second, lattice strain and dielectric performance have not been comprehensively analyzed. Understanding these mechanisms is essential for developing low-loss, thermally stable, and energy-efficient dielectric ceramics.

In this study, we investigate a series of $[(Mg_{1-x}Co_x)_{0.95}Zn_{0.05}]TiO_3$ ceramics (x = 0.1–0.4) synthesized via a conventional solid-state reaction method. The influence of Co^{2+} substitution on phase formation, microstructure, and dielectric behavior is systematically examined by combining synchrotron X-ray diffraction (XRD), Raman spectroscopy, scanning electron microscopy (SEM), and microwave dielectric characterization. Particular attention is given to identifying optimal sintering conditions that minimize secondary phase formation and thermal budget. The results reveal that the composition $[(Mg_{0.8}Co_{0.2})_{0.95}Zn_{0.05}]TiO_3$, sintered at 1350 °C for 2 h, offers a balanced combination of high *Qf* (190,000 GHz), moderate permittivity (ε_r = 18.42), and stable τ_f (−51 ppm/°C), along with a 43.7% reduction in thermal budget compared to previous reports.

Unlike previous works that focused on Co doping at single sintering conditions, this study provides a systematic phase–property correlation across both compositional and thermal variables, offering a more comprehensive framework for microwave dielectric ceramic optimization. While Co and Zn co-doping has been previously reported, this study uniquely focuses on optimizing *Qf* under reduced thermal budgets while retaining phase stability, addressing industrial fabrication challenges. This work provides new insights into the interplay between structural evolution and dielectric performance in Co-modified $MgTiO_3$ ceramics and provides a sustainable route for designing next-generation microwave dielectric materials for 5G/B5G applications.

Experimental Procedure

Material Preparation

In this study, $(Mg_{1-x}Co_x)_{0.95}Zn_{0.05}TiO_3$ (hereafter referred to as MCZT) ceramics were synthesized using a conventional solid-state reaction method. High-purity oxide powders—MgO, ZnO, CoO, and TiO_2—were mixed according to precise stoichiometric calculations. MgO powder was pre-fired at 600 °C for 2 hours to reduce moisture absorption. The mixed powders were then ball-milled in distilled water with agate balls for 24 hours, followed by drying and calcination at 1000 °C for 3 hours in a high-temperature furnace. A binder comprising 3.5 wt% of a 12% PVA (polyvinyl alcohol) solution was incorporated into the calcined powders, which were subsequently granulated using a 100-mesh sieve. The granulated material was pressed into pellets with a diameter of 11 mm and a thickness of 5 mm under a pressure of 200 MPa.

Sintering Process

The MCZT pellets were sintered in an air atmosphere, with sintering conditions optimized by varying the temperature (1275–1375 °C) and duration (1–4 hours). The heating and cooling rates of the furnace were carefully controlled at approximately 10 °C/min to ensure uniform heating and minimize thermal gradients across the samples. This controlled approach ensured consistent microstructure development and optimized the microwave dielectric performance of the ceramics.

Characterization Techniques

A range of analytical techniques was employed to evaluate the structural, morphological, and dielectric properties of the MCZT ceramics:

Crystallographic Analysis

X-ray diffraction (XRD) using a Siemens D5000 instrument was utilized to examine the crystallization states of the calcined powders and sintered materials. The lattice constants were determined by fitting the XRD patterns using the Rietveld method.

Microstructure Observation

Scanning electron microscopy (SEM; Philips XL-40FEG) was used to observe the microstructures of the sintered surfaces, while energy-dispersive X-ray spectroscopy (EDS) was employed to identify any secondary phases.

Density Measurement

The apparent density of the sintered ceramics was measured using Archimedes' method, and relative densities were calculated.

The theoretical density was calculated based on the weighted average of component phases using the rule of mixtures. For the dominant perovskite $[(Mg_{1-x}Co_x)_{0.95}Zn_{0.05}]TiO_3$, the unit cell volume was estimated from XRD data, assuming a pseudocubic lattice.

Microwave Property Evaluation

Dielectric constant and quality factor at microwave frequencies were measured using the Hakki-Coleman dielectric resonator method [34, 35]. A vector network analyzer (Anritsu MS46122B) was used to characterize microwave properties.

Temperature Coefficient of Resonance Frequency (τ_f)

Temperature coefficient of resonance frequency (τ_f) measurements were conducted using the same setup within a thermostat, varying from 20 to 80 °C. The τ_f value (ppm/°C) was calculated using formula (1):

$$\tau_f = \frac{f_2 - f_1}{f_1(T_2 - T_1)} \quad (1)$$

f_1 and f_2 represent the resonance frequencies at $T_1 = 20$ °C and $T_2 = 80$ °C, respectively.

Results and Discussion

Fig. 1 presents the X-ray diffraction (XRD) patterns

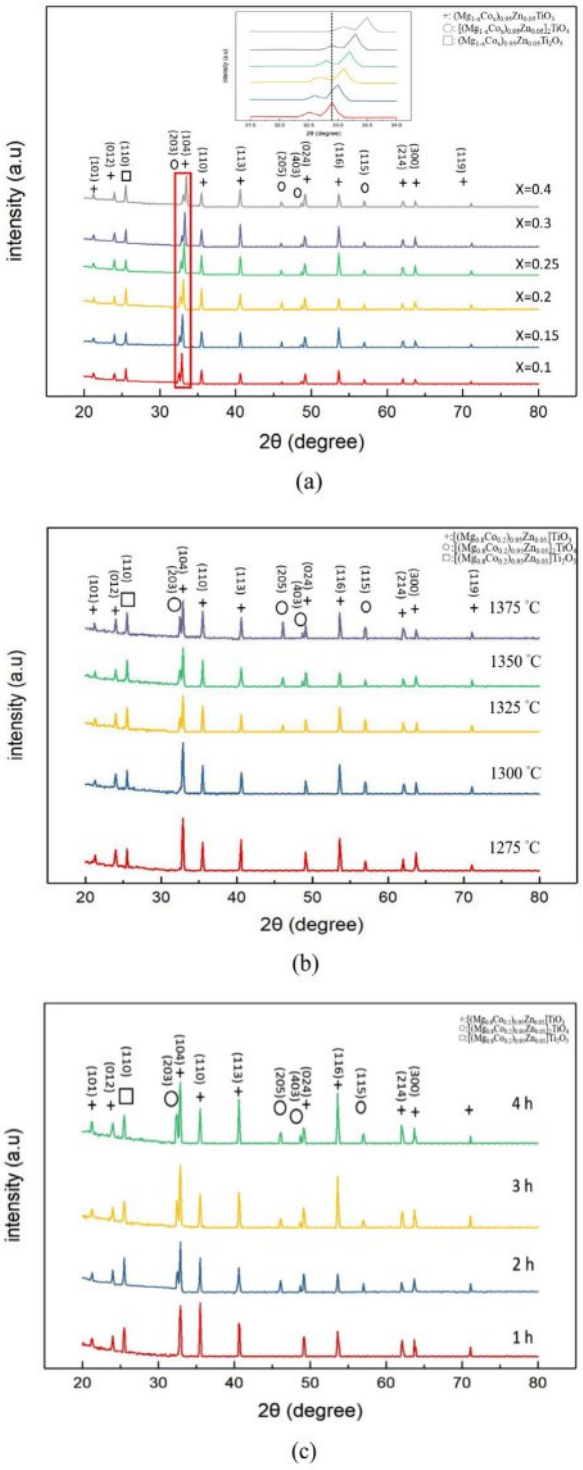

Fig. 1. X-ray diffraction patterns of $[(Mg_{1-x}Co_x)_{0.95}Zn_{0.05}]TiO_3$ ceramics (a) with various x compositions sintered at 1350 °C for 2 h, (b) different sintering temperatures for 2 h under $x = 0.2$, and (c) sintering at 1350 °C with varying times under $x = 0.2$.

of $[(Mg_{1-x}Co_x)_{0.95}Zn_{0.05}]TiO_3$ ceramics under different sintering conditions and compositions. Fig. 1(a) shows that increasing Co content (x = 0.1 to 0.4) leads to discernible structural changes in the XRD patterns. The diffraction peaks at lower substitution levels ($x = 0.1$–0.2) remain sharp and well-defined, indicating a dominant perovskite phase with orthorhombic symmetry. The main reflections, indexed as (101), (110), and (203), do not exhibit significant positional deviation. However, when x exceeds 0.2, peak broadening and a slight shift toward higher 2θ values are observed, indicating lattice contraction and increased microstrain within the crystal matrix is attributed to the replacement of smaller Mg^{2+} ions (0.72 Å) with Co^{2+} (0.74 Å), introducing local distortions and compositional disorder.

The inset of Fig. 1(a), focusing on the 2θ range between 31.5° and 34°, further confirms a gradual shift in peak positions with increasing Co content, indicative of unit cell modifications and strain accumulation. These observations are consistent with solid solution formation at low Co contents and incipient secondary phase development at higher doping levels. The XRD peaks were indexed based on ICDD-PDF #00-006-0494 for the primary $MgTiO_3$ phase.

Fig. 1(b) illustrates the phase evolution of the optimal composition $[(Mg_{0.8}Co_{0.2})_{0.95}Zn_{0.05}]TiO_3$ sintered at various temperatures for 2 h. The XRD patterns exhibit clean single-phase features at lower temperatures (≤1300 °C). However, with increasing sintering temperature, additional peaks emerge, corresponding to secondary phases—specifically $[(Mg_{0.8}Co_{0.2})_{0.95}Zn_{0.05}]_2TiO_4$ and $[(Mg_{0.8}Co_{0.2})_{0.95}Zn_{0.05}]Ti_2O_5$—as indexed by ICDD-PDF #00-025-1157 and #00-035-0792. This observation suggests that excessive thermal energy promotes compositional inhomogeneity and secondary phase segregation, which have been reported to deteriorate dielectric performance in similar $MgTiO_3$-based systems [29].

Fig. 1(c) illustrates the time-dependent crystallization behavior of the optimized composition at a fixed sintering temperature of 1350 °C. As the sintering time increases from 1 h to 2 h, the primary perovskite reflections—such as (110), (203), and (300)—become sharper and more intense, indicating grain growth and improved crystallinity. Upon extending the sintering duration to 3 h and 4 h, additional peaks emerge and intensify, corresponding to secondary phases. Specifically, reflections at (203), (205), (403), and (115), marked with □, are indexed to $[(Mg,Co)_2]TiO_4$, while the (110) reflection marked with ○ corresponds to $[(Mg,Co)]Ti_2O_5$. These developments suggest that prolonged sintering promotes secondary phase segregation and compositional instability, potentially degrading the dielectric performance.

Table 1 summarizes the refined lattice parameters of $[(Mg_{1-x}Co_x)_{0.95}Zn_{0.05}]TiO_3$ ceramics (x = 0 to 0.4) sintered at 1350 °C for 2 h. The results confirm the formation of

Table 1. Lattice constants of $[(Mg_{1-x}Co_x)_{0.95}Zn_{0.05}]TiO_3$ ceramics different x compositions sintered at 1350 °C for 2 h.

Composition in x	a = b (Å)	c (Å)
$(Mg_{0.95}Zn_{0.05})TiO_3$	5.0557	13.9029
$[(Mg_{0.9}Co_{0.1})_{0.95}Zn_{0.05}]TiO_3$	5.0554	13.9025
$[(Mg_{0.85}Co_{0.15})_{0.95}Zn_{0.05}]TiO_3$	5.0551	13.9016
$[(Mg_{0.8}Co_{0.2})_{0.95}Zn_{0.05}]TiO_3$	5.0548	13.9011
$[(Mg_{0.75}Co_{0.25})_{0.95}Zn_{0.05}]TiO_3$	5.0545	13.8999
$[(Mg_{0.7}Co_{0.3})_{0.95}Zn_{0.05}]TiO_3$	5.0542	13.8992
$[(Mg_{0.6}Co_{0.4})_{0.95}Zn_{0.05}]TiO_3$	5.0541	13.8987

a continuous solid solution with orthorhombic symmetry. As Co content increases, the lattice constants a and c exhibit a slight but consistent contraction—from a = 5.5057 Å and c = 13.9029 Å at $x = 0$ to a = 5.0541 Å and c = 13.8987 Å at $x = 0.4$. This trend reflects the influence of ionic substitution and defect chemistry, where lattice shrinkage is governed by local distortions caused by Co incorporation and oxygen vacancy compensation mechanisms.

The ionic radii referenced in this study were based on Shannon's effective ionic radius table [34], where Mg^{2+} (0.72 Å, VI coordination), Co^{2+} (0.74 Å) are commonly reported. These values provide a theoretical foundation for the observed trend of lattice contraction as Co content increases. Although Rietveld refinement was not conducted in this study, the progressive shift in XRD peaks and monotonic decrease in lattice parameters confirm solid solution formation and structural evolution. Further work involving full-profile refinement could provide a more quantitative analysis of multiphase proportions and lattice distortions.

Overall, the XRD results demonstrate that Co substitution into $Mg_{0.95}Zn_{0.05}TiO_3$ can effectively tailor the crystal structure but also carries the risk of forming deleterious secondary phases at elevated temperatures or prolonged sintering durations. Therefore, fine-tuning the sintering conditions is essential for stabilizing the desired perovskite phase and suppressing phase decomposition. These findings form a structural basis for the subsequent analysis of dielectric performance.

The microstructure of $[(Mg_{1-x}Co_x)_{0.95}Zn_{0.05}]TiO_3$ ceramics was examined using scanning electron microscopy (SEM), and elemental distribution was analyzed via energy-dispersive X-ray spectroscopy (EDS), as shown in Figs 2 and 3. For the optimal composition $[(Mg_{0.8}Co_{0.2})_{0.95}Zn_{0.05}]TiO_3$ sintered at 1350 °C for 2 h, the fractured surfaces reveal a dense, polycrystalline morphology with well-developed grains. The grain boundaries are clearly defined, and intergranular porosity is minimal, indicating effective densification.

Microstructural evolution with varying sintering temperatures (Fig. 2g–j) further supports these observations. At lower temperatures (e.g., 1275 °C), incomplete densification and residual porosity are evident. As temperature increases to 1350 °C, the grain size becomes more uniform, and the overall density is maximized. However, at 1375 °C, abnormal grain coarsening and pore growth occur, indicating over-sintering-induced grain boundary migration and potential phase decomposition.

Similarly, time-dependent sintering behavior (Fig. 2k–m) reveals that optimal grain morphology is achieved at 2 h, while extended sintering (≥3 h) leads to exaggerated grain growth and irregular grain shapes. These phenomena harm dielectric performance by introducing microstructural inhomogeneity and increasing dielectric loss.

To further quantify the microstructural evolution with sintering temperature, the grain-size distributions of the optimized $[(Mg_{0.8}Co_{0.2})_{0.95}Zn_{0.05}]TiO_3$ were analyzed at 1275 °C, 1300 °C, 1325 °C, 1350 °C, and 1375 °C for 2 h, as shown in Fig. 2(n). Each dataset was obtained from 30–50 grains measured on SEM micrographs. The average grain size increased steadily from ≈ 3 μm at 1275 °C to ≈ 15 μm at 1375 °C, indicating progressive densification and grain growth with rising temperature. Meanwhile, the distribution became narrower at 1350 °C, suggesting the formation of a more homogeneous microstructure with reduced porosity. This quantitative analysis confirms that 1350 °C yields the most uniform and well-developed perovskite grains, consistent with the optimized microstructure observed in SEM images.

Fig. 3 and Table 2 display EDS point analysis of $[(Mg_{0.8}Co_{0.2})_{0.95}Zn_{0.05}]TiO_3$ sintered at 1350 °C for 2 h on selected grains labeled A–D. Spots A and B correspond to the primary $[(Mg_{0.8}Co_{0.2})_{0.95}Zn_{0.05}]TiO_3$ phase and exhibit higher Ti and Mg content, consistent with the target composition. Spot C, which shows significantly higher oxygen and lower cation content, is likely indicative of a Ti-rich secondary phase such as $[(Mg_{0.8}Co_{0.2})_{0.95}Zn_{0.05}]Ti_2O_5$, potentially forming in localized regions with compositional inhomogeneity. Spot D, enriched in Mg and Co but deficient in Ti, suggests the presence of a $[(Mg_{0.8}Co_{0.2})_{0.95}Zn_{0.05}]_2TiO_4$-type secondary phase. These compositional variations confirm the occurrence of minor phase segregation in select grains, particularly at higher sintering temperatures or prolonged dwell times.

Overall, the SEM and EDS analyses highlight the importance of precisely controlling sintering temperature and dwell time to suppress secondary phase formation and maintain microstructural uniformity. The optimized microstructure of $[(Mg_{0.8}Co_{0.2})_{0.95}Zn_{0.05}]TiO_3$—characterized by dense packing, uniform grains, and minimal porosity—contributes directly to the excellent dielectric properties discussed in the subsequent sections.

The secondary phases were identified through a combination of synchrotron XRD and EDS analyses (Figs. 1(b) and 3). The main reflections correspond to the ilmenite-type $(Mg,Co,Zn)TiO_3$ phase, while minor peaks marked in Fig. 1(b) were attributed to spinel-type $[(Mg,Co,Zn)_2TiO_4]$ and Ti-rich $[(Mg,Co,Zn)Ti_2O_5]$

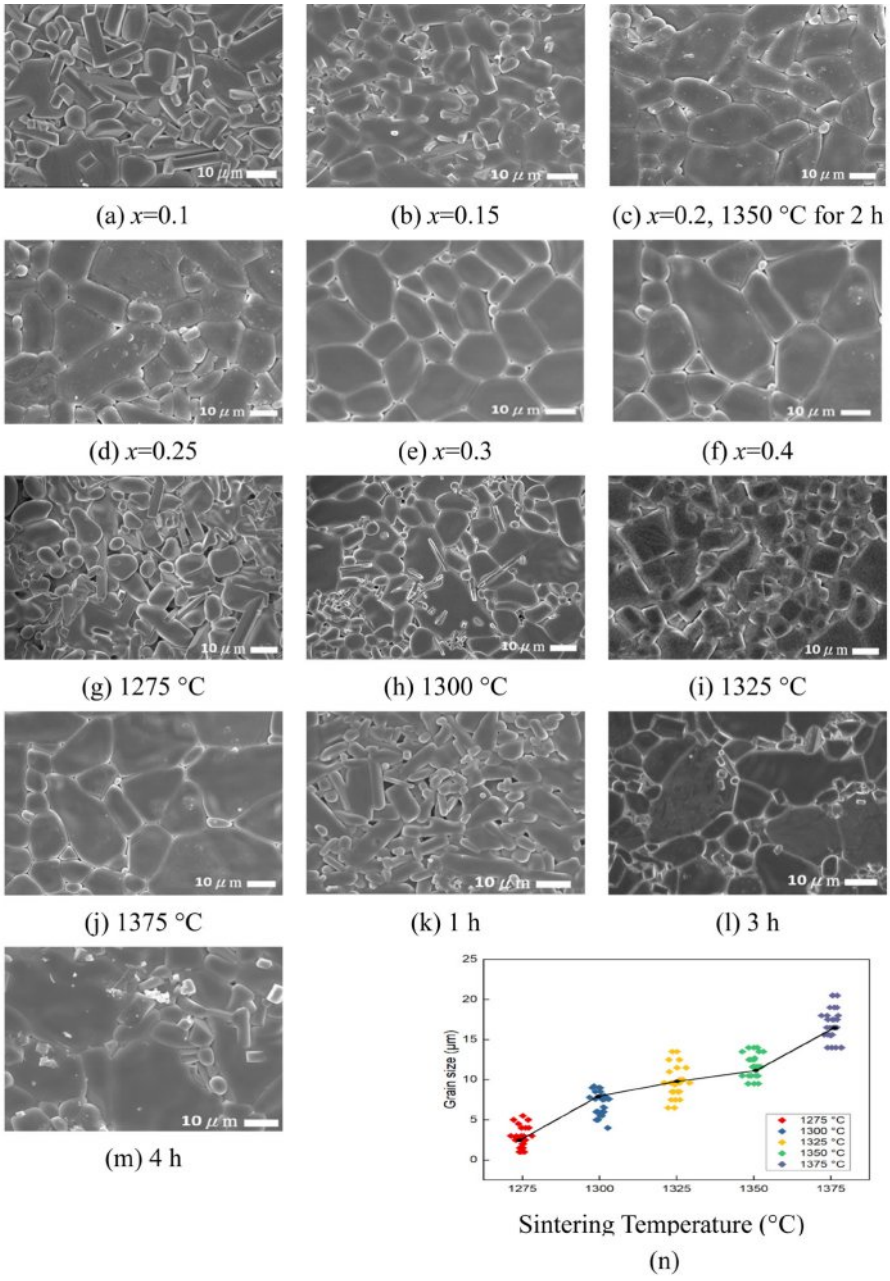

Fig. 2. Scanning electron microscopy photographs ceramics (a)–(f) $[(Mg_{1-x}Co_x)_{0.95}Zn_{0.05}]TiO_3$ with various x values sintered at 1350 °C for 2 h, (g)–(j) $[(Mg_{0.8}Co_{0.2})_{0.95}Zn_{0.05}]TiO_3$ with various sintering temperature for 2 h, (k)–(m) $[(Mg_{0.8}Co_{0.2})_{0.95}Zn_{0.05}]TiO_3$ with various sintered time at 1350 °C, (n) Grain-size distribution of $[(Mg_{0.8}Co_{0.2})_{0.95}Zn_{0.05}]TiO_3$ sintered at different temperatures for 2 h and the solid line indicates the average grain size at each temperature.

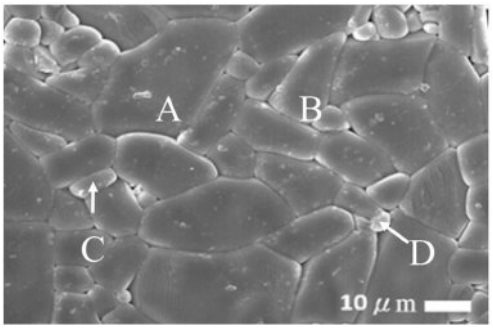

Fig. 3. EDS photograph of $[(Mg_{0.8}Co_{0.2)0.95}Zn_{0.05}]TiO_3$ ceramics at 1350 °C for 2 h.

Table 2. The EDS results of $[(Mg_{0.8}Co_{0.2})_{0.95}Zn_{0.05}]TiO_3$ ceramics at 1350 °C for 2 h.

Spot	Atom(%)				
	Mg	Co	Zn	Ti	O
A	17.27	3.82	1.42	26.42	51.06
B	20.18	4.16	1.34	25.38	48.99
C	12.31	1.37	0.42	23.01	62.88
D	23.56	5.07	1.66	15.55	56.44

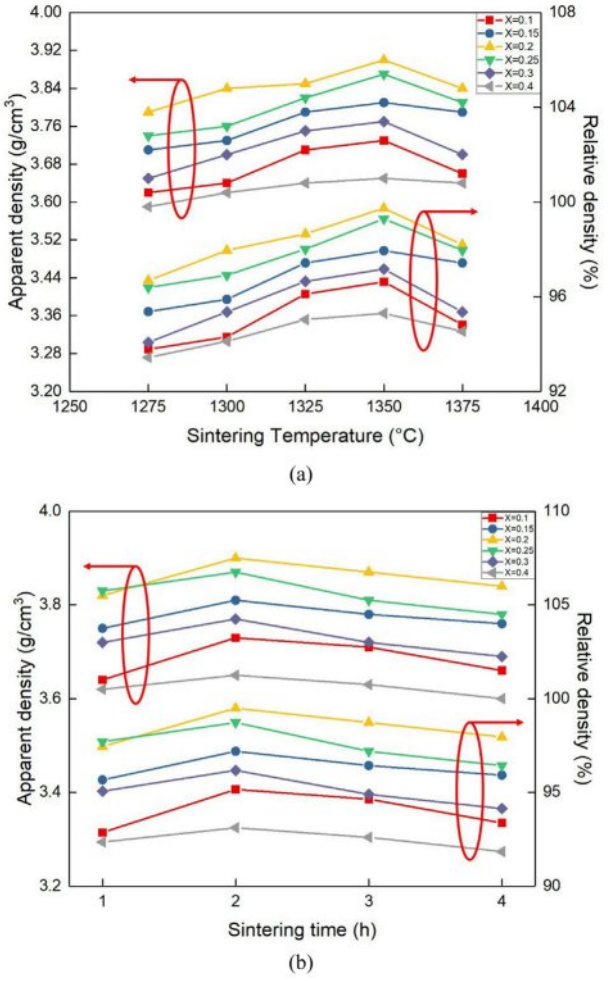

Fig. 4. Apparent density and relative density of $[(Mg_{1-x}Co_x)_{0.95}Zn_{0.05}]TiO_3$ with x=0–0.4 as a function of (a) sintering temperature and (b) time.

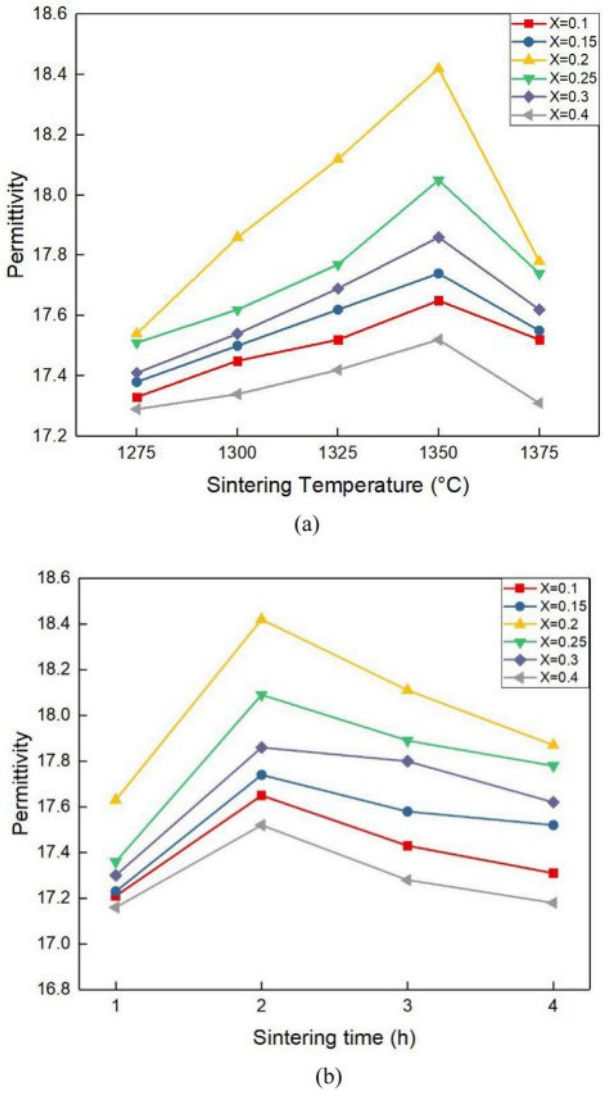

Fig. 5. Permittivity of $[(Mg_{1-x}Co_x)_{0.95}Zn_{0.05}]TiO_3$ with x=0–0.4 as a function of (a) sintering temperature and (b) time.

phases, based on comparison with ICDD #25-1157 and #35-0792, respectively. EDS mapping and spot analyses further confirmed this assignment: areas A and B in Fig. 3 exhibited near-stoichiometric (Mg,Co,Zn)TiO_3 composition, whereas areas C and D showed Ti-rich or Mg/Co-enriched signals consistent with the Ti_2O_5- and $(Mg,Co)_2TiO_4$-type phases. The estimated volume fraction of these secondary phases, derived from the integrated XRD peak intensities, remained below ≈ 5 % for samples sintered at 1350 °C and increased slightly to ≈ 8–10% at 1375 °C. These results indicate that minor phase segregation occurs only under over-sintered conditions, while phase purity is largely maintained at the optimized 1350 °C/2 h condition.

Figs. 4 through 7 illustrate the densification behavior and dielectric performance of $[(Mg_{1-x}Co_x)_{0.95}Zn_{0.05}]TiO_3$ ceramics as sintering temperature, time, and Co content.

Fig. 4 presents both the apparent and relative densities as functions of (a) sintering temperature (1275–1375 °C, fixed time of 2 h) and (b) sintering time (1–4 h at 1350 °C). The data show that densification improves with increasing temperature and time up to an optimal point. The highest apparent density (3.90 g/cm³) and relative density (~99.6%) were achieved at 1350 °C for 2 h with x = 0.2. Beyond this point, further increases in temperature or sintering duration led to a decline in density, likely due to abnormal grain growth and the formation of intergranular voids. These results confirm that excessive thermal input can induce microstructural coarsening, counteracting densification, and potentially introducing scattering centers that degrade dielectric performance.

Dielectric permittivity (ε_r) trends are shown in Fig. 5(a) and 5(b). For all compositions, permittivity increases with sintering temperature and time, reaching a peak at 1350 °C for 2 h. The maximum value (ε_r = 18.42) was observed for x = 0.2. Beyond this point, further sintering reduces ε, which is attributed to grain coarsening and the emergence of secondary phases that

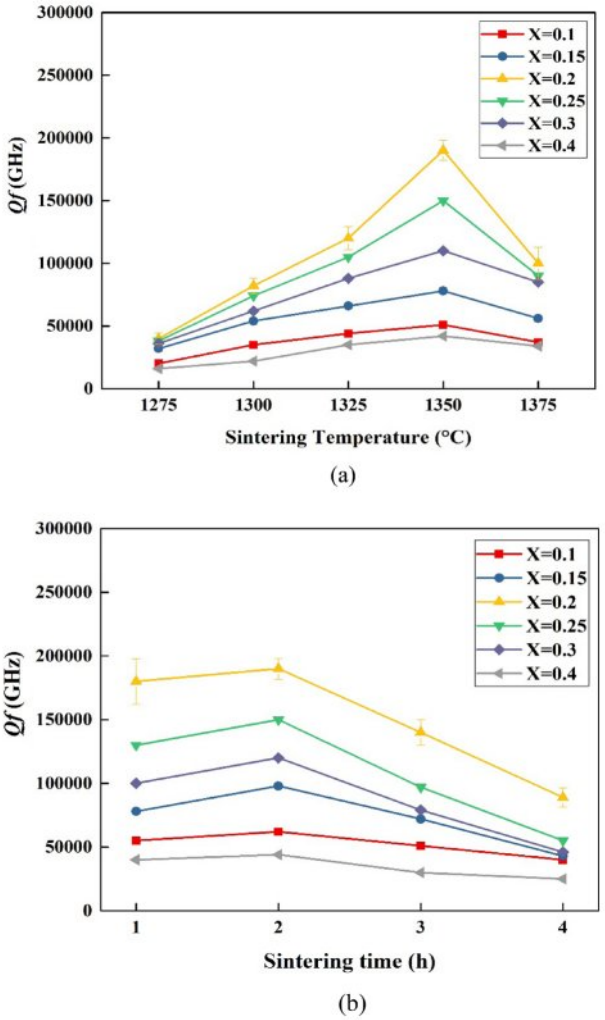

Fig. 6. Quality factor of $[(Mg_{1-x}Co_x)_{0.95}Zn_{0.05}]TiO_3$ ceramics (x = 0–0.4) as a function of (a) sintering temperature and (b) sintering time. Error bars represent the standard deviation from three independent sintering batches.

disrupt the uniform polarization response. According to the Clausius–Mosotti equation

$$\varepsilon_r = \frac{3V_m + 8\pi\alpha_m}{3V_m - 4\pi\alpha_m} \quad (2)$$

The relative permittivity is affected by molecular polarizability (α_m) and molar volume (V_m) [36]. These parameters were derived for each composition, suggesting that enhanced polarizability under optimal conditions is linked to suppressed porosity and improved grain connectivity.

Fig. 6(a) and 6(b) depict the variation in quality factor (*Qf*) for different Co contents (x = 0.1–0.4) as a function of sintering temperature (1275–1375 °C for 2 h) and sintering time (1–4 h at 1350 °C). The results show that *Qf* improves with increased sintering temperature and time, reaching a maximum of approximately 190,000 GHz for $[(Mg_{0.8}Co_{0.2})_{0.95}Zn_{0.05}]TiO_3$ sintered at 1350 °C for 2 h. This condition represents the optimal balance between densification, grain growth, and phase stability, yielding the best dielectric performance among all tested compositions. To evaluate the reproducibility and reliability of the dielectric data, each *Qf* value was obtained from three independently sintered pellets under identical conditions. The resulting variations were within ±3–7 %, depending on the sintering temperature and dwell time. The error bars in Fig. 6 represent the standard deviation of these repeated measurements. The optimized sample (x = 0.2, 1350 °C/2 h) exhibited the highest *Qf* (~190,000 GHz) and the smallest deviation (±3%), confirming excellent batch-to-batch consistency.

Beyond the 2-hour sintering duration or at temperatures exceeding 1350 °C, *Qf* begins to decline, which is attributed to microstructural degradation such as abnormal grain growth, increased porosity, and the formation of secondary phases. These changes introduce dielectric loss pathways that compromise energy storage and reduce overall performance.

Notably, compositions with higher Co content (x ≥ 0.3) exhibit significantly lower *Qf* values. This degradation correlates with the emergence of secondary phases—specifically $[(Mg_{0.8}Co_{0.2})_{0.95}Zn_{0.05}]_2TiO_4$ and $[(Mg_{0.8}Co_{0.2})_{0.95}Zn_{0.05}]Ti_2O_5$—which form at grain boundaries and create interfacial polarization losses. These phases also decrease relative density, further exacerbating dielectric degradation.

In contrast, at x = 0.2, secondary phase formation is minimal, enabling a clean microstructure dominated by the primary perovskite phase. This leads to enhanced permittivity (ε = 18.42) and outstanding *Qf* values, making it highly suitable for microwave applications.

These results underscore the critical importance of controlling both Co concentration and sintering protocol to suppress undesirable phase formation and maintain microstructural integrity. Precise optimization at x = 0.2 and 1350 °C for 2 h ensures the highest dielectric quality, supporting the use of this material in high-frequency, low-loss device applications.

Fig. 7 illustrates the temperature coefficient of resonant frequency (τ_f) for $[(Mg_{1-x}Co_x)_{0.95}Zn_{0.05}]TiO_3$ ceramics with different Co contents (x = 0.1–0.4) as functions of sintering temperature and sintering time. Fig. 7(a) shows the τ_f values over a temperature range of 1275 to 1375 °C (2 h sintering), while Fig. 7(b) presents the dependence on sintering duration (1–4 h at 1350 °C). The results demonstrate that τ_f values for all compositions remain consistently negative, ranging from approximately −55 to −47 ppm/°C.

Among all compositions, x = 0.2 exhibits the most favorable thermal stability, with a τ_f of approximately −51 ppm/°C at 1350 °C for 2 h. This composition offers excellent dielectric performance (as shown in previous sections) and provides a well-balanced thermal response suitable for practical device applications. In contrast, higher Co contents ($x \geq 0.3$) tend to yield slightly less

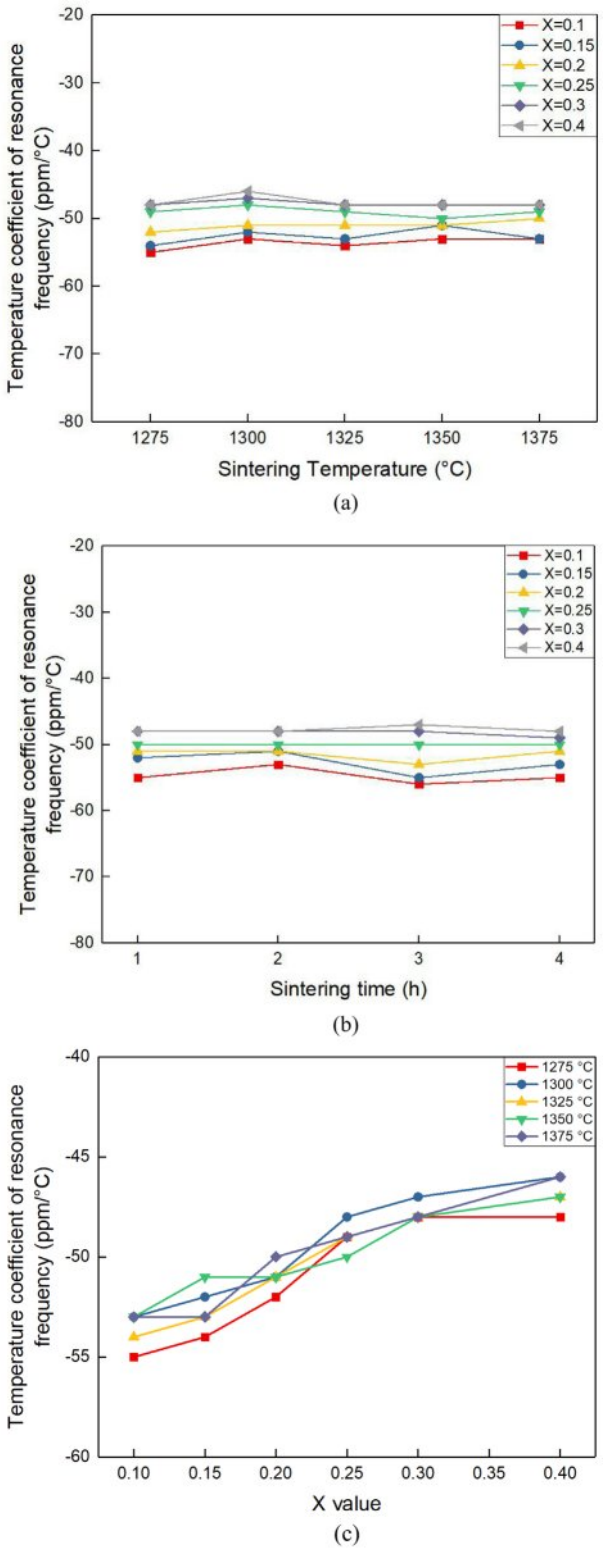

Fig. 7. Temperature coefficient of the resonant frequency of $[(Mg_{1-x}Co_x)_{0.95}Zn_{0.05}]TiO_3$ with x=0–0.4 as a function of (a) sintering temperature and (b) time, (c) with various sintering temperatures for 2 h as a function of x value.

negative τ_f values, indicating a marginal improvement in temperature stability; however, this comes at the cost of reduced *Qf* and microstructural degradation.

Fig. 7(c) further confirms the trend that increasing Co content gradually shifts τ_f toward less negative values. This behavior is attributed to modifications in crystal structure and polarizability associated with Co incorporation and related oxygen vacancy dynamics.

Generally speaking, the tunability of τ_f in most cases is governed by the temperature coefficient of permittivity (τ_ε) and the thermal expansion coefficient (α_l) [3], as described by Eq. (3):

$$\tau_f = \alpha_l + \frac{1}{2}\tau_\varepsilon \quad (3)$$

In many ceramic systems, τ_f is predominantly influenced by τ_ε, as α_l is typically an order of magnitude smaller and can be considered negligible. Therefore, improvements in τ_f are closely linked to the stabilization of dielectric polarization mechanisms and the minimization of structural asymmetries that affect τ_ε.

Overall, the data reveal that $[(Mg_{0.8}Co_{0.2})_{0.95}Zn_{0.05}]TiO_3$ provides the optimal balance among permittivity, quality factor, and τ_f. Its reliable thermal response, with high *Qf* and minimal secondary phase formation, highlights its potential for temperature-stable microwave dielectric applications.

Fig. 8 displays the Raman spectra of $[(Mg_{1-x}Co_x)_{0.95}Zn_{0.05}]TiO_3$ ceramics (x = 0.1–0.4) sintered at 1350 °C for 2 h. The spectra exhibit several Raman-active modes characteristic of the ilmenite-type TiO_6 octahedra. The peaks near 225 cm^{-1} (A_1g), 285 cm^{-1} (E_1g), 330–340 cm^{-1} (E_2g/E_3g), and 470 cm^{-1} (A_4g) correspond to Ti–O–Ti bending and octahedral tilting vibrations, whereas the broad band at 610–710 cm^{-1} (E_5g/A_5g) arises from Ti–O symmetric stretching [7, 38].

As Co^{2+} substitution increases, the E_1g (~285 cm^{-1}) mode becomes sharper, more intense, and slightly blue-shifted, signifying enhanced octahedral distortion and stronger local strain fields. For higher Co concentrations (x ≥ 0.3), slight peak broadening is observed, implying a degree of structural disorder or defect-related distortion within the TiO_6 framework. This trend agrees with the XRD and SEM analyses, indicating that excessive Co incorporation perturbs the lattice regularity. Overall, moderate Co^{2+} substitution (x = 0.2) optimizes the octahedral environment and polarizability, resulting in superior dielectric performance in $[(Mg_{1-x}Co_x)_{0.95}Zn_{0.05}]TiO_3$ ceramics.

Table 3 summarizes the systematic optimization of microwave dielectric properties in $[(Mg_{1-x}Co_x)_{0.95}Zn_{0.05}]TiO_3$ ceramics as a function of Co content (x = 0–0.4) under fixed sintering conditions of 1350 °C for 2 h. The results provide a clear comparison of how compositional tuning influences key performance metrics, including dielectric constant (ε_r), quality factor (*Qf*), and temperature coefficient of resonant frequency (τ_f).

Among all compositions, x = 0.2 emerges as the optimal formulation, exhibiting ε_r = 18.42, *Qf* = 190,000 GHz, and τ_f = −51 ppm/°C. These values represent a

Table 3. Dielectric properties in detail of $[(Mg_{1-x}Co_x)_{0.95}Zn_{0.05}]TiO_3$ ceramics with optimized sintering temperature 1350 °C for 2 h under x=0.4.

x value	$[(Mg_{1-x}Co_x)_{0.95}Zn_{0.05}]TiO_3$				
	S.T./Time (°C/ h)	Density (g/cm^3)	Permittivity	*Qf* (GHz)	τ_f (ppm/°C)
0	1300 /4	3.91	16.21	240,000	−60
0.1	1350 /2	3.73	17.65	51,000	−53
0.15	1350 /2	3.81	17.74	78,000	−52
0.2	1350 /2	3.90	18.42	190,000	−51
0.25	1350 /2	3.87	18.05	150,000	−50
0.3	1350 /2	3.77	17.86	110,000	−48
0.4	1350 /2	3.65	17.52	42,000	−47

synergistic balance of high permittivity, low dielectric loss, and stable temperature behavior. The superior performance of this composition is attributed to its dense and homogeneous microstructure, minimal porosity, and the effective suppression of secondary phases.

The data also reinforce that secondary phase formation, particularly $[(Mg_{0.8}Co_{0.2})_{0.95}Zn_{0.05}]_2TiO_4$ and $[(Mg_{0.8}Co_{0.2})_{0.95}Zn_{0.05}]Ti_2O_5$, is closely correlated with excessive Co doping ($x \geq 0.3$). While these phases may introduce localized polarization sites, their presence increases interfacial scattering, grain boundary density, and structural inhomogeneity, ultimately degrading dielectric performance.

Therefore, precise control over the doping concentration and sintering parameters is critical. The results from Table 3 establish a process–structure–property framework, highlighting how moderate Co substitution (x = 0.2) enables the realization of optimal dielectric functionality. These findings provide a strategic foundation for further refinement of $MgTiO_3$-based ceramics targeted for high-frequency, energy-efficient microwave applications.

To evaluate the processing efficiency of the optimized composition, the thermal budget during sintering was calculated and compared with previously reported formulations. The thermal budget is defined as the product of sintering temperature and holding time, which serves as a first-order approximation of total energy input during processing.

For the reference composition $[(Mg_{0.7}Zn_{0.3})_{0.95}Co_{0.05}]TiO_3$ reported by Huang et al., sintered at 1200 °C for 4 h, the thermal budget is:

Thermal Budget (MZCT) = 1200 °C × 4 h = 4800 °C·h

In comparison, the optimized composition $[(Mg_{0.8}Co_{0.2})_{0.95}Zn_{0.05}]TiO_3$ in this study was sintered at 1350 °C for 2 h:

Thermal Budget (MCZT) = 1350 °C × 2 h = 2700 °C·h

The percentage reduction in the thermal budget is calculated as:

$$\text{Thermal Budget Reduction (\%)} = (4800 - 2700)/4800 \times 100 \approx 43.7\% \quad (4)$$

Despite the slightly lower dielectric constant (ε_r = 18.42 vs. 20.0), the current composition exhibits a significantly enhanced quality factor (*Qf* = 190,000 GHz vs. 163,560 GHz; +16.2%) and a more thermally stable temperature coefficient of resonance frequency (τ_f = −51 ppm/°C vs. −65 ppm/°C). This trade-off favors overall device performance, particularly in systems with prioritized low dielectric loss and thermal stability. Table 4 provides a direct comparison of these key metrics. The results demonstrate that the current composition

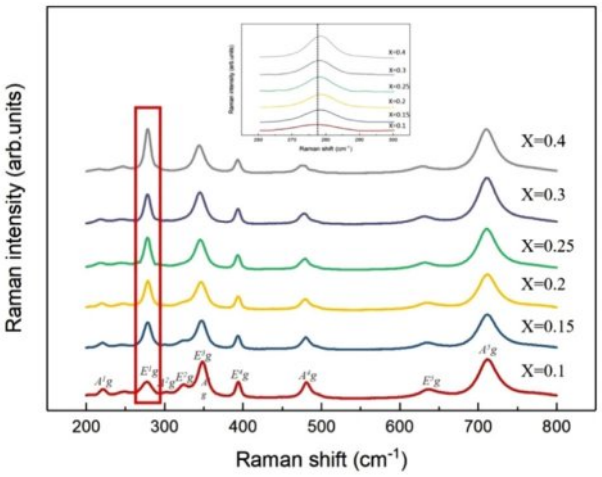

Fig. 8. Raman analysis of $[(Mg_{1-x}Co_x)_{0.95}Zn_{0.05}]TiO_3$ (x=0.1–0.4) sintered at 1350 °C for 2 h.

Table 4. Comparison of the proposed optimized dielectrics with similar documented dielectrics.

Composition	S.T./Time (°C/ h)	Permittivity	*Qf* (GHz)	τ_f (ppm/°C)	Ref.
$MgTiO_3$	1400/4	17	160,000	−50	[29]
$[(Mg_{0.7}Zn_{0.3})_{0.95}Co_{0.05}]TiO_3$	1200 /4	20.0	163,560	−65	[33]
$[(Mg_{0.8}Co_{0.2})_{0.95}Zn_{0.05}]TiO_3$	1350 /2	18.42	190,000	−51	This work

meets performance benchmarks and substantially reduces energy consumption, enhancing its potential for environmentally sustainable, large-scale production.

The long-term stability of the optimized composition was also examined. Samples stored under ambient conditions for several months exhibited no detectable change in XRD patterns, and repeated dielectric measurements showed variations within ±3%, confirming stable phase and electrical behavior. Similar stabilization effects of Co^{2+} incorporation in $MgTiO_3$-based ceramics were shown to enhance lattice stability [32, 33].

Conclusion

This study systematically investigated the effects of cobalt (Co) substitution for magnesium (Mg) on the structure, microstructure, and microwave dielectric performance of $[(Mg_{1-x}Co_x)_{0.95}Zn_{0.05}]TiO_3$ ceramics. Through comprehensive analysis of phase composition, Raman-active vibrational modes, oxidation states, and sintering behavior, the work revealed that both Co content and sintering parameters critically influence dielectric performance. The optimized composition $[(Mg_{0.8}Co_{0.2})_{0.95}Zn_{0.05}]TiO_3$, sintered at 1350 °C for 2 h, exhibited superior microwave dielectric properties with a quality factor (*Qf*) of 190,000 GHz, a dielectric constant (ε_r) of 18.42, and a temperature coefficient of resonant frequency (τ_f) of −51 ppm/°C. Compared to previously reported compositions, this formulation demonstrates a 16.2% improvement in *Qf* while maintaining competitive ε_r and offering a τ_f closer to zero, indicating enhanced thermal stability.

Moreover, the proposed processing route reduces the thermal budget by approximately 43.7% relative to earlier studies, underscoring the potential for energy-efficient fabrication. This balance between high performance and low thermal demand addresses key challenges, including energy consumption and environmental sustainability. The comprehensive optimization of dielectric properties, phase purity, and microstructural uniformity provides a robust framework for developing next-generation microwave dielectric ceramics. The optimized $[(Mg_{0.8}Co_{0.2})_{0.95}Zn_{0.05}]TiO_3$ composition, combining a high *Qf* value and stable dielectric constant, demonstrates strong potential for integration into microwave components such as dielectric resonators, antennas, and 5G bandpass filters. Future work will focus on incorporating temperature-compensation layers to achieve near-zero τ_f and on implementing 3.5 GHz filter prototypes based on this ceramic substrate. These findings validate the efficacy of Co substitution in tailoring material properties and establish a guiding strategy for the future design of low-loss, thermally stable, and sustainable ceramic materials.

Acknowledgment

The authors gratefully acknowledge the financial support from the National Science and Technology Council (NSTC), Taiwan, under Grant Nos. NSTC 112-2221-E-224-018-MY2, NSTC 114-2221-E-224-031, and NSTC 114-2222-E-224-018. This work was also supported by the National Yunlin University of Science and Technology through Project No. 114-3026-1, funded in collaboration with LiveStrong Optoelectronics Company. The authors also thank LiveStrong Optoelectronics Company for their valuable technical assistance and experimental support.

Data Availability

The data used in this study are available from the author upon reasonable request.

Conflict of interest

The authors declare that they have no conflict of interest.

ORCID

Shih-Hung Lin https://orcid.org/0000-0001-5982-6905

References

1. H. Yu, T. Luo, and J. Liu, Adv. Appl. Ceram. 118 (2019) 98-105.
2. H. Li, H. Liu, L. Li, F. Liu, K.-C. Chang, and S. Liu, J. Alloys Compd. 1010 (2025) 177190.
3. G. Yao, Y. Li, J. Tan, C. Pei, Y. Zhang, and J. Chen, J. Ceram. Process. Res. 21[3] (2020) 338-342.
4. P. Palmero, Nanomaterials 5 (2015) 656-696.
5. A. Naeem, A. Ullah, Y. Iqbal, T. Mahmood, A. Mahmood, and Z.A. Razaa, J. Alloys Compd. 672 (2016) 298-306.
6. S. Promsai, J. Boonlakhorn, and P. Srepusharawoot, Materialia 32 (2023) 101899.
7. Y.-C. Chen, R.-Y. Syu, and X.-F. Ding, Ceram. Int. 43 (2017) S301-S305.
8. S. Kim, C.-B. Hong, S.-H. Kwon, and S.-O. Yoon, J. Ceram. Process. Res. 18[6] (2017) 421-424.
9. S.-H. Lin, Z.-Q. Lin, and C.-W. Chen, Ceram. Int. 47 (2021) 16828-16832.
10. S.-H. Lin, Z.-Q. Lin, and Y.-R. Wu, ECS J. Solid State Sci. Technol. 10 (2021) 073008.
11. B. Itaalit, M. Mouyane, J. Bernard, M. Womes, and D. Houivet, Appl. Sci. 6 (2016) 2.
12. S. Zhai, P. Liu, and Z. Fu, J. Mater. Sci. Mater. Electron. 29 (2018) 1298-1303.
13. Q. Yang, T. Luo, T. Yu, and H. Yu, J. Mater. Sci. Mater. Electron. 31 (2020) 15184-15191.
14. W.-S. Xia, W.-H. Zhang, Y. Wang, M.-X. Li, L.-W. Shi, and H.-T. Wu, J. Mater. Sci. Mater. Electron. 33 (2022) 8027-8034.
15. S. Yuan, L. Gan, F. Ning, S. An, J. Jiang, and T. Zhang, Ceram. Int. 44 (2018) 20566-20569.
16. B. Tang, Q. Xiang, Z. Fang, X. Zhang, Z. Xiong, H. Li, C. Yuan, and S. Zhang, Ceram. Int. 45 (2019) 11484-11490.
17. J.-H. Sohn, Y. Inaguma, S.-O. Yoon, M. Itoh, T. Nakamura, S.-J. Yoon, and H.-J. Kim, Jpn. J. Appl. Phys. 33 (1994) 5466.
18. C. Du, M.-S. Fu, D. Zhou, H.-H. Guo, H.-T. Chen, J. Zhang, J.-P. Wang, S.-F. Wang, H.-W. Liu, W.-F. Liu, L. Li, and Z. Xu, J. Am. Ceram. Soc. 104 (2021) 4659-4668.

19. J. Zhang, Z. Yue, Y. Luo, and L. Li, Ceram. Int. 44 (2018) 21000-21003.
20. L. Li, S. Li, X. Lyu, H. Sun, and J. Ye, Mater. Lett. 163 (2016) 51-53.
21. A. Manan, Z. Ullah, A.S. Ahmad, A. Ullah, D.F. Khan, A. Hussain, and M.U. Khan, J. Adv. Ceram. 7 (2018) 72-78.
22. Q. Du, J. Duan, L. Ma, L. Jiang, and H. Li, J. Eur. Ceram. Soc. 44 (2024) 5639-5645.
23. F. Lin, Y. Lai, B. Li, Y. Li, W. Gong, Q. Zhang, M. Xie, and C. Wu, Ceram. Int. 49 (2023) 40374-40381.
24. C.-E. Huang, Z. Wang, and J. Yang, Ceram. Int. 50 (2024) 48869-48878.
25. Z. Ren, F. Zeng, C. Yuan, F. Liu, J. Zhao, B. Zhu, C. Zhou, J. Xu, and G. Rao, Ceram. Int. 50 (2024) 9861-9868.
26. C.-H. Shen and C.-L. Huang, J. Alloys Compd. 472 (2009) 451-455.
27. L. He, H. Yu, M. Zeng, E. Li, J. Liu, and S. Zhang, J. Electroceram. 40 (2018) 360-364.
28. A. Ullah, Y. Iqbal, T. Mahmood, A. Mahmood, A. Naeem, and M. Hamayun, Ceram. Int. 41 (2015) 15089-15096.
29. H.-J. Jo, J.-S. Kim, and E.-S. Kim, Ceram. Int. 41 (2015) S530-S536.
30. Y.-S. Park and E.-S. Kim, J. Ceram. Process. Res. 23[6] (2022) 920-926.
31. G.-G. Yao and P. Liu, J. Ceram. Process. Res. 13[3] (2012) 235-238.
32. C.-L. Huang, Y.-B. Chen, and S.-H. Lin, J. Alloys Compd. 477 (2009) 712-715.
33. C.-L. Huang, S.-H. Lin, S.-S. Liu, Y.-B. Chen, and S.-Y. Wang, J. Alloys Compd. 503 (2010) 392-396.
34. W.E. Courtney, IEEE Trans. Microwave Theory Tech. 18 (1970) 476-485.
35. R. D. Shannon and C.T. Prewitt, Acta Crystallogr. 25 (1969) 925-946.
36. I.-T. Kim, Y. Kim, and S.-J. Chung, Jpn. J. Appl. Phys. 34 (1995) 4096.
37. X. Yuan, X. Xue, F. Jin, and H. Wang, J. Eur. Ceram. Soc. 39 (2019) 4156-4159.
38. C.-H. Wang, X.-P. Jing, W. Feng, and J. Lu, J. Appl. Phys. 104 (2008) 034112.